ACS OMEGA

http://pubs.acs.org/journal/acsodf

Article

Auxetic Carbon Honeycomb: Strain-Tunable Phase Transitions and Novel Negative Poisson's Ratio

Yanchun Li, Shuaiwei Wang,* and Baocheng Yang*

Cite This: *ACS Omega* 2021, 6, 14896−14902

Read Online

ACCESS | Metrics & More | Article Recommendations | Supporting Information

ABSTRACT: Auxetic structure and tunable phase transitions are fascinating properties for future application. Herein, we propose two three-dimensional (3D) carbon honeycombs (CHC), known as *Cmcm*-CHC and *Cmmm*-CHC. Based on first-principles calculations, these novel 3D materials exhibit auxeticity with a fascinating negative Poisson's ratio, which stems from (i) the puckered structure of *Cmcm*-CHC along the tube axis and (ii) significant change of angle-dominant deformation for *Cmmm*-CHC in the armchair direction. In addition, the moderate strain drives semimetal to semiconductor phase transition in CHCs, which thoroughly establishes its C−C bond formation. In the meantime, two new phases, namely $P6_3/mmc$-CHC and $P6/mmm$-CHC, form and exhibit semiconductor characteristics. Our results also show that *Cmcm*-CHC and $P6_3/mmc$-CHC are superhard materials. The outstanding negative Poisson's ratio and phase transition properties make CHCs highly versatile for innovative applications in microelectromechanical and nanoelectronic devices.

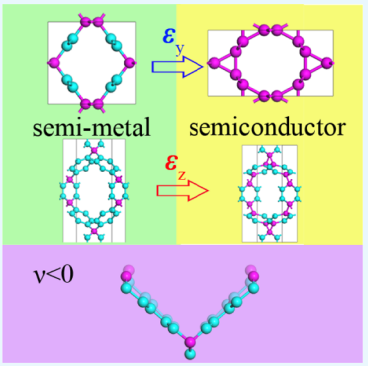

INTRODUCTION

Since the discovery of graphene in 2004,[1] the field of carbon-based material has attracted tremendous interest. Due to the unique ability of carbon to form sp^1 and sp^2 as well as sp^3 hybridization states, a series of two-dimensional (2D) and three-dimensional (3D) carbon allotropes were identified and studied.[2−7] These materials exhibit a variety of structural and remarkable electronic, thermal, optical, and mechanical properties.[8−13] Especially, 3D carbon honeycomb[5,6,14] materials have been extensively researched.

Recently, the 3D carbon honeycomb (CHC) has been successfully synthesized by experimental research.[6] The CHC structure has a regular channel structure with sp^2-bonded carbon atoms and exhibits high levels of physical absorption than carbon nanotubes and fullerenes. However, imaginary phonon modes were observed in CHCs by theoretical calculations.[14] Therefore, some new structures of CHCs with Dirac[15] and Weyl semimetal[5] characteristics were predicted with ultrahigh Fermi velocity. Besides the fascinating electronic band structure, the carbon materials also display outstanding mechanical properties, especially a negative Poisson's ratio (NPR). NPR materials with typical auxetic features exhibit a counterintuitive behavior: they expand when stretched and contract when compressed. Due to their unique mechanical properties, auxetic materials have been attracting increasing attention from researchers. The first auxetic material was manufactured in 1987.[16] In the past years, the computational model of an auxetic molecular system was first computed by Monte Carlo simulations,[17] and then the static version of a two-dimensional molecular model was rigorously solved by Wojciechowski.[18] Evans et al. proposed the re-entrant 2D auxetic networks.[19] Tretiakov et al. reported a rapid decrease of Poisson's ratio in 2D hard body systems by Monte Carlo simulation.[20] For the carbon-based materials, either modifying the cell shape or altering the bond length can possibility induce the NPR phenomena in single-walled carbon nanotubes.[21] Furthermore, the NPR phenomena occur in graphene at a small strain and independent of the size and temperature,[22] or by introduction of vacancy defects.[23] The NPR for single-layer graphene ribbons was found at widths smaller than 10 nm.[24] In addition, metals with periodic porous structures can also show a NPR.[25] Hence, it is of great interest to explore the mechanical properties of novel 3D CHC materials, especially for their structural and property response by applying an external strain, which may offer key insights into their fundamental mechanisms and potential for application in nanodevices.

In this paper, the mechanical properties of two 3D CHCs are investigated by first-principles calculations. Our results reveal that the CHCs exhibit auxeticity (negative Poisson's ratio) under tensile loading and superhard properties. The NPR phenomena in CHCs originate from the puckered structure and angle bending. Remarkably, the strain-induced semimetal to semiconductor transformation in CHCs is mainly due to the new C−C bond forming. The excellent mechanical

Received: February 8, 2021
Accepted: April 12, 2021
Published: May 28, 2021

coupled with highly tunable electronic properties make 3D CHCs a promising material for nanoscale devices.

RESULTS AND DISCUSSION

Figure 1 presents the top, side, and perspective views of the atomic structure of *Cmcm*-CHC and *Cmmm*-CHC, in which

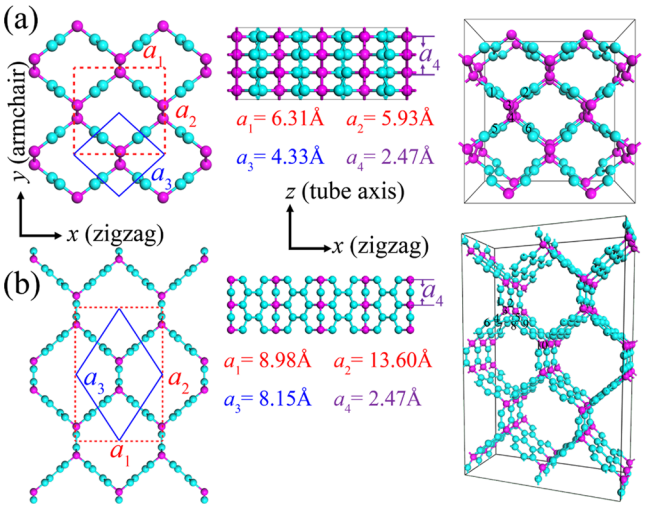

Figure 1. Optimized atomic structures of (a) *Cmcm*-CHC and (b) *Cmmm*-CHC from top, side, and perspective views along *x* (zigzag), *y* (armchair), and *z* (tube) directions. The blue/red box represents the basic unit cell/calculation model of the CHC structure. The pink and blue carbon atoms are sp^3-hybridized and sp^2-hybridized, respectively.

the sp^3-hybridized carbon atoms (pink) are linked with three nanoribbons by the sp^2-hybridized carbon atoms (blue). The optimized structural parameters are shown in Figure 1. For the *Cmcm*-CHC, the carbon atoms occupied the 8*g* (0.70 0.22 1.25) and 4*c* (0.5 0.07 1.25) positions. For the *Cmmm*-CHC, the carbon atoms occupied the 8*q* (0.78 0.81 0.5), 8*p* (0.82 0.87 0.0), 4*g* (0.61 0.5 0.0), and 4*h* (0.55 0.5 0.5) positions. In our previous study,[15] the *Cmcm*-CHC and *Cmmm*-CHC structures showed either thermal stability or mechanical stability. The strain is defined as $\varepsilon_i = (a - a_{0i})/a_{0i}$ (i = x, y, z), where a_{0i} is the lattice constant. The Poisson's ratios under tensile loading along the x direction were calculated[26] using the formula $\nu_{xj} = -\partial\varepsilon_j/\partial\varepsilon_x$, ($j$ = y, z). The details of the computational method are given in Section I of the Supporting Information.

Negative Poisson's Ratio. Having established the structure configurations of CHCs, we now focus on the structural response under uniaxial loading and evaluate the resulting Poisson's ratios. The Poisson's ratios of CHCs are shown in Figure 2 for uniaxial deformation along the *x* (zigzag) and *z* (tube axis) directions. The strain of *Cmcm*-CHC along the *y* (armchair) axis (Figure 2a) exhibits approximate linearization in the tensile deformation region, as indicated by the positive Poisson's ratio. Remarkably, the lattice constant along the *z* (tube axis) direction first shrinks and then expands by the tensile strain in the *x* (zigzag) direction. By using a quartic fit, the Poisson's ratio can be obtained from Figure 2a. The value of Poisson's ratio is shown in Figure 2b as a function of the strain. The Poisson's ratio along the tube axis is negative at strains larger than 0.27 in the zigzag direction. At large strains, with growing strain the absolute value of the negative Poisson's ratio becomes smaller. For instance, the Poisson's ratio along the tube axis is 0.034(−0.015) at a strain of 0.1(0.3). It should be noted that the negative Poisson's ratio (NPR) phenomenon also appeared along the tube axis (zigzag direction) during its deformation along the armchair direction (tube axis) (Figure S1) and no NPR phenomenon occurs along the tube axis. Different from *Cmcm*-CHC, the strain for *Cmmm*-CHC along the *y* axis (armchair) reveals a monotonic increase, while the *x* axis shows a positive Poisson's ratio during its deformation along the *z* axis. Figure 2d shows that the NPR of *Cmmm*-CHC expands along the *y* (armchair) axis when stretched along the *z* (tube) axis, whereas the Possion's ratio undergoes changes in three stages (first decreases at strains <0.05, then tending to keep a constant value at strains from 0.05 to 0.14, and then dropping sharply at strains >0.14). The NPR is about −0.632 at a strain of 0.21 along the armchair direction, which is larger than that of *Cmcm*-CHC. As shown in Table 1, the NPR of *Cmcm*-CHC is lower than most of other materials,[27−34] whereas the NPR of *Cmmm*-CHC is larger than that of other 3D carbon-based materials,[28,29] similar to 2D carbon-based materials[27,30,33] and other materials.[31,32,34] In short, the Poisson's ratios are dependent on the deformation, which means that the Poisson's ratio of CHCs is not a constant in the elastic stage and that it is a function of strain.

Mechanisms of Negative Poisson's Ratio. We next unveil the NPR mechanisms by examining the atomic configurations. Figure 3 shows the deformation modes to gain further insight into the relationship between the structure and NPR mechanisms, where the arrows represent the direction of atomic movement. Two deformation processes are found for *Cmcm*-CHC. In process I (ε_x < 0.27), atoms 1, 2, 5, and 6 move along the *x* axis (blue arrow) as shown in Figure 3a; meanwhile, the increasing angles of ∠132 and ∠546 induce atoms 1, 2, 5, and 6 to move up/down along the *y* axis (Figure 3b) and the distances d_1 and d_2 decrease/increase as shown in Figure 3g. So, no NPR phenomenon is found in process I. In process II (ε_x> 0.27), d_1 increases with increase in the strain, which induces the relative motion of atoms 3 and 4 (red arrow) as shown in Figure 3c along the *y* axis, so d_2 decreases. The effect of the movement of atoms 3 and 4 results in the NPR appearing along the *z* axis. These results indicate that the angle and bond length elongate to accommodate the external tension, leading to the NPR phenomenon along the tube axis for *Cmcm*-CHC. Compared with *Cmcm*-CHC, only one process is observed for *Cmmm*-CHC. Atoms 1, 2, 5, and 6 move along the *z* axis as shown in Figure 3d, with the tensile strain along the tube axis, whereas the surrounding atoms 3, 4, and 7 adjust their position along the *x* and *y* axis (red arrows in Figure 3e,f). Therefore, the lattice constant along the *y* axis increases, inducing the NPR phenomenon. For example, the angles of ∠546 and ∠132 are 121.71 and 112.32° at a strain ε_z = 0.0; a larger increase (with d_1 decreasing) of the angles ∠546 = 128.09° and ∠132 = 118.75° is found at a strain ε_z = 0.10. Therefore, the length from atom 3 to atom 10 slightly changes from 5.89 to 5.83 Å (atom 10 in Figure 1b). As a consequence of the movement of atoms 3, 4, and 7 (red online), the angle ∠437 decreases (with d_2 increasing) from 101.34 to 98.38°. In contrast, the variations for the angles are larger than for the bond length, so the angle-dominant deformation process leads to the NPR phenomenon.

Strain-Induced Phase Transformation. The stress−strain response of CHCs is shown in Figure 4 for different directions. At smaller strains, a linear relationship is found for

https://doi.org/10.1021/acsomega.1c00718
ACS Omega 2021, 6, 14896−14902

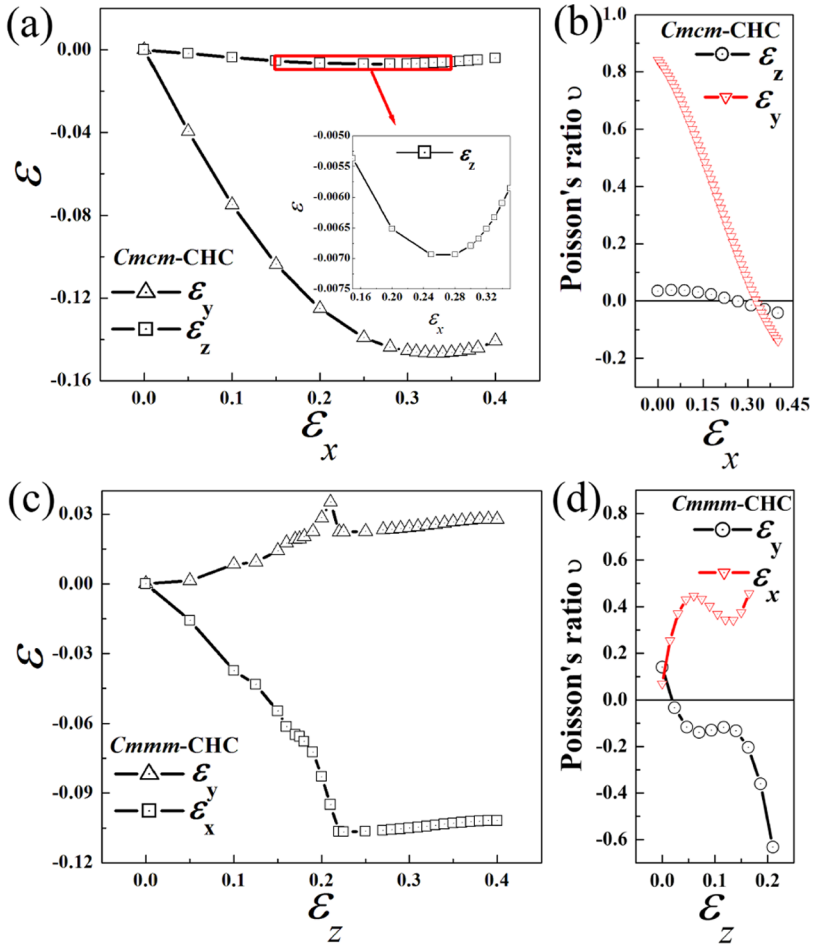

Figure 2. Poisson's ratio as a function of the uniaxial deformation of *Cmcm*-CHC and *Cmmm*-CHC structures. (a) Strain ε_x versus ε_y and ε_z for the *Cmcm*-CHC structure subjected to uniaxial tensile loading in the zigzag direction. (b) Poisson's ratio of the *Cmcm*-CHC structure along the tube axis. (c) Strain ε_z versus ε_y and ε_x for *Cmmm*-CHC structure subject to uniaxial tensile loading along the tube axis. (d) Poisson's ratio of the *Cmmm*-CHC structure in the armchair direction.

Table 1. Comparison of the Poisson's Ratio of CHCs with Those of Some Previously Reported Materials

structures		υ_x	υ_y	υ_z	
3D carbon-based materials	*Cmcm*-CHC			0.038∼−0.042	strain-induced
	Cmmm-CHC		0.14∼−0.63		
	bco-C20[28]		∼−0.13		
	carbon honeycomb[29]			−0.32	
2D carbon-based materials	Penta-graphene[27]	−0.068	−0.068		intrinsic
	Xgraphene[30]	0.18∼−0.053			strain-induced
	tetrahex C[33]	0.04∼−0.081	0.036∼−0.127		
	graphene[22]		0.3∼−0.04		
other materials	B_4N[31]	−0.018	−0.032		intrinsic
	Ag_2S[32]		−0.12	−0.54	
	gallium thiophosphate[34]		−0.033	−0.62	

Cmcm-CHC in the armchair, zigzag, and tube directions. As the strain increases, the stress moves to a plastic region until the structure breaks in the armchair and zigzag directions. The tensile strengths (strain) are 62 GPa (0.28) along the armchair direction, 88 GPa (0.35) along the zigzag direction, and 137 GPa (0.26) along the tube axis. It should be noted that the tensile strength of *Cmcm*-CHC in the tube axis is larger than that of graphene (113 GPa) in the armchair direction.[35] Compared with *Cmcm*-CHC, the stress−strain response of *Cmmm*-CHC exhibits a nonlinear relationship in the armchair and zigzag directions due to the angle increase being greater than that of bond length at small strains. The tensile strengths are about 68 GPa (0.35), 53 GPa (0.49), and 81 GPa (0.21) along the armchair, zigzag, and tube axes, respectively. Interestingly, the stress quickly drops for *Cmcm*-CHC at a strain of 0.28 in the armchair direction and 0.22 for *Cmmm*-CHC in the tube axis. These intriguing stress variations indicate the structure reconstructions and transitions in CHCs.

In order to explore the structural transition under uniaxial loading, the bonding configuration and structural evolution of CHCs under strain loading are illustrated in Figure 5. The distance d_1 of the C1−C2 atom decreases linearly at strains

https://doi.org/10.1021/acsomega.1c00718
ACS Omega 2021, 6, 14896−14902

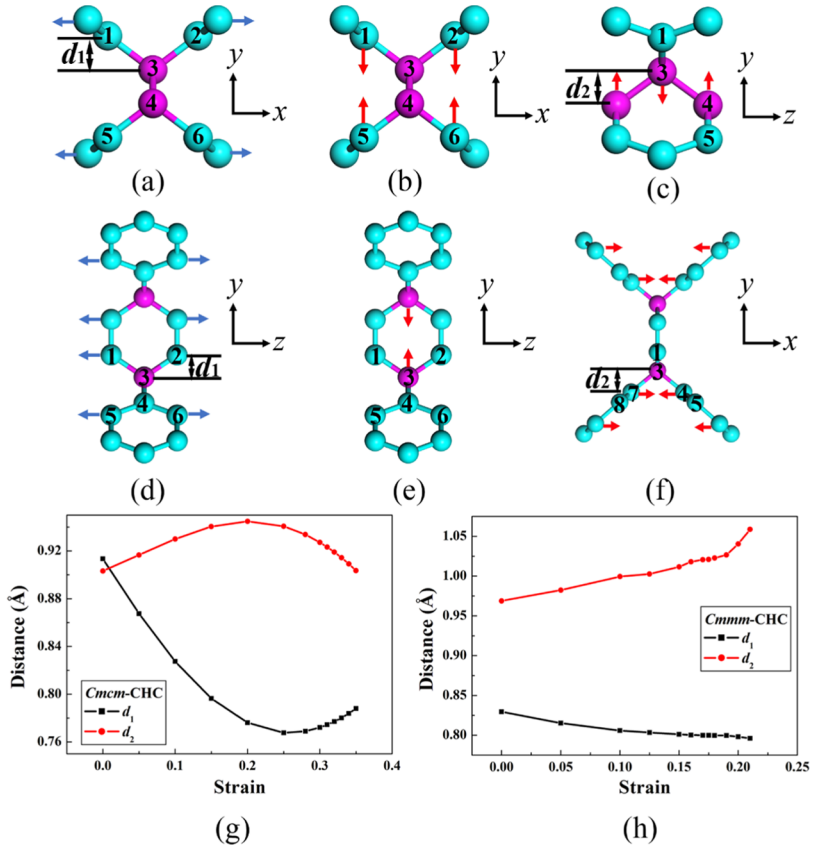

Figure 3. Deformation mechanism for NPR. The blue arrows indicate the movement direction of the atoms by stretching along the zigzag direction of (a) *Cmcm*-CHC and tube axis of (d) *Cmmm*-CHC structure. The atomic positions along the *y* and *z* axis for (b, c) *Cmcm*-CHC and *x* and *y* axis for (e, f) *Cmmm*-CHC are shown. The red arrows display the movement direction after tensile loading. (g, h) Distances d_1 and d_2 as a function of strain.

from 0.0 to 0.28. The distance d_1 is 1.51 Å at a strain of 0.30, which is close to the C−C single bond distance, indicating a new bond formation. The space group of *Cmcm*-CHC changes from the original *Cmcm* to $P6_3/mmc$. This new structure has been predicted in a previous study.[36] On further loading in the armchair direction, the bond length d_2 breaks at strain 0.46 and the structure spontaneously transforms into the initial phase (*Cmcm*-CHC). The evolution of the bond lengths d_1, d_2, and angle θ are shown in Figure 5c. For uniaxial tension along the tube axis for *Cmmm*-CHC, both the bond lengths d_1, d_2, and angle θ show a significant change at strain 0.21, which is similar to the case for *Cmcm*-CHC. The structure transforms to another phase at strains larger than 0.21. In this process, the distance d_1 shrinks as the strain increases in the zigzag direction and leads to the movement of C1 and C2 atoms close to each other, thus forming a new C−C bond in the zigzag direction. This is the main reason for a sharp drop in the stress as shown in Figure 4b. Different from *Cmcm*-CHC, there is no new phase at larger strains for *Cmmm*-CHC, except for the *Cmmm* phase to *P6/mmm* phase transformation. The phonon dispersions of two phases ($P6_3/mmc$-CHC and *P6/mmm*-CHC) are calculated to examine their stability. As shown in Figure S2, the absence of an imaginary frequency demonstrates the dynamic stability of $P6_3/mmc$-CHC and *P6/mmm*-CHC after the structural transition.

We illustrate the crystal structures of $P6_3/mmc$-CHC and *P6/mmm*-CHC in the inset of Figure 5c,d. The details of the crystal structures, including lattice parameters, space group, bond length, and cohesive energy, are shown in Table S1. However, the most fascinating feature of $P6_3/mmc$-CHC and *P6/mmm*-CHC is their electronic property. The electronic band structures of $P6_3/mmc$-CHC and *P6/mmm*-CHC at its equilibrium state and strain are presented in Figure 6. Figure 6a demonstrates a semiconducting phase with a direct band gap of 2.256 (1.554) eV at a strain of 0.0 (0.31) at the Γ point, which is close to the band gap of silicon[37] and black phosphorene.[38] There are three low energy bands at the band edges. One nondegenerate conduction band and two valence bands degenerate at the Γ point. Under the tensile strain, the conduction moves down, while the two valence bands slightly change. Interestingly, *P6/mmm*-CHC shows metallicity at a strain of 0.0, while an indirect-gap semiconductor shows an indirect band gap of about 0.887 eV at a strain of 0.31. As shown in Figure 5c,d, both *Cmcm*-CHC and *Cmmm*-CHC transition from semimetal to semiconductor phase under external strain and remain stable and robust against environmental perturbations. The results will definitely motivate and provide useful guidance for designing and applying these exciting phenomena in nanodevices.

Bulk Moduli (*B*), Shear Moduli (*G*), Young's Moduli, and Vickers Hardness. The mechanical properties, including bulk moduli (B), shear moduli (G), and Young's moduli (E), of the CHCs are calculated (Table 2). The B and G values for *Cmcm*-CHC are 313 and 289 GPa, respectively, which are derived using the Voigt method[39,40] and are given by $B = (1/9)[C_{11} + C_{22} + C_{33} + 2(C_{12} + C_{13} + C_{23})]$ and $G = (1/15)[C_{11} + C_{22} + C_{33} + 3(C_{44} + C_{55} + C_{66}) - (C_{12} + C_{13} + C_{23})]$. The results show that *Cmcm*-CHC has high resistance to fracture

https://doi.org/10.1021/acsomega.1c00718
ACS Omega 2021, 6, 14896−14902

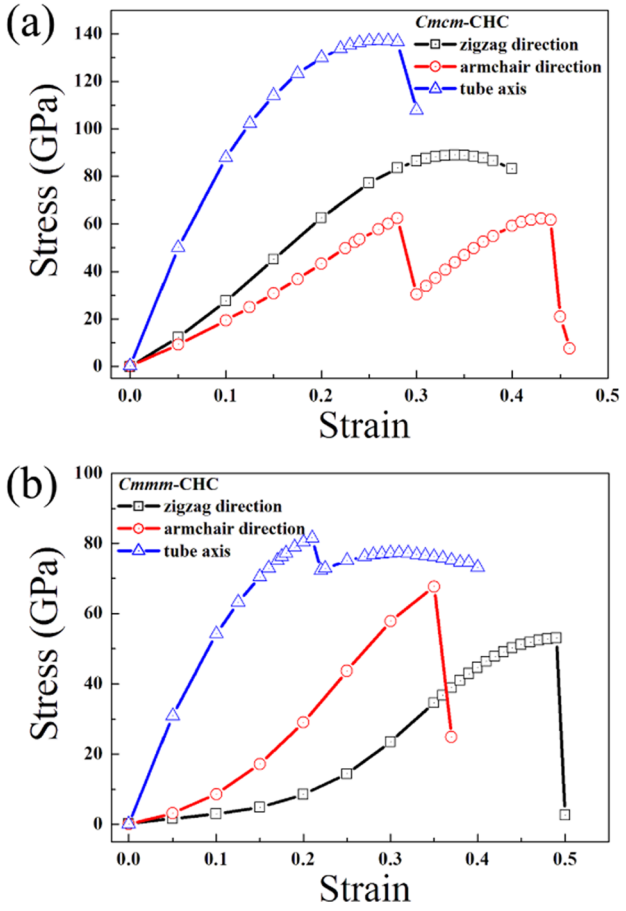

Figure 4. Strain−stress curve of (a) *Cmcm*-CHC and (b) *Cmmm*-CHC.

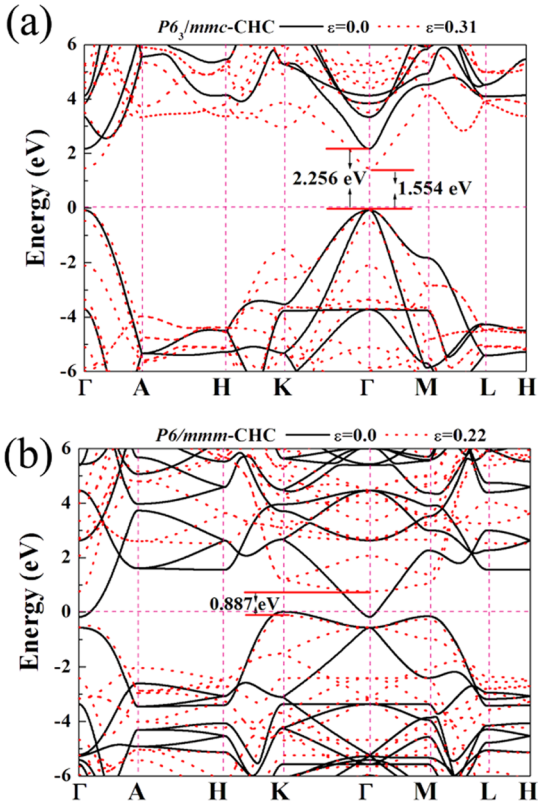

Figure 6. Band structures of (a) $P6_3/mmc$-CHC and (b) *P6/mmm* -CHC structures at different strains.

and weak plastic deformation. Note that the *B* and *G* of *Cmcm*-CHC and *Cmmm*-CHC are lower than those of diamond (*B*

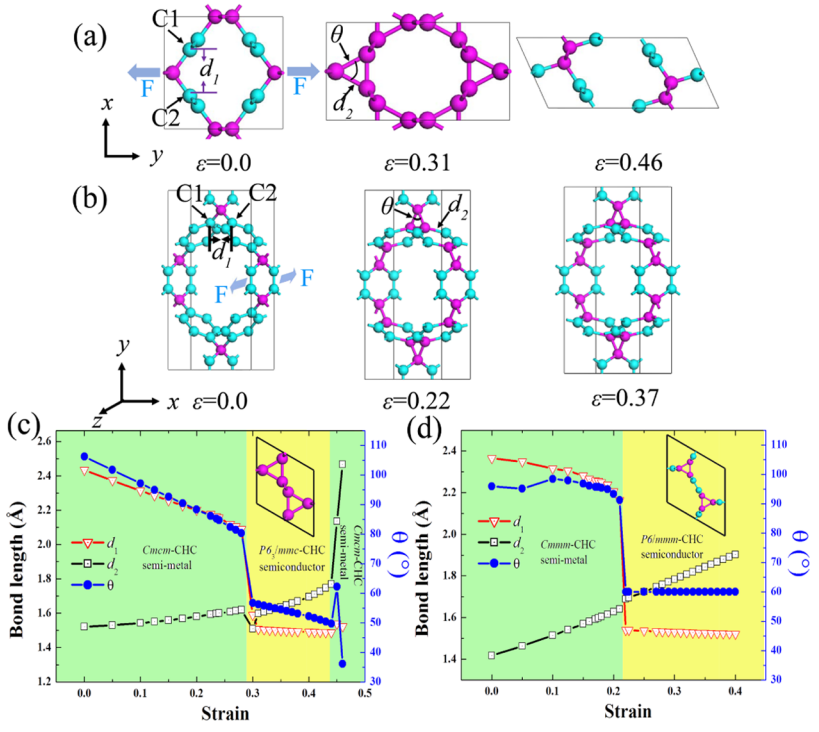

Figure 5. Structure evolution under uniaxial tensile loading for (a) *Cmcm*-CHC and (b) *Cmmm*-CHC structures at different strains. The bond length and bond angle as a function of strain for (c) *Cmcm*-CHC and (d) *Cmmm*-CHC structures. The upper inset picture in (c) and (d) shows the unit cell of a new structure under tensile loading.

https://doi.org/10.1021/acsomega.1c00718
ACS Omega 2021, 6, 14896−14902

Table 2. Bulk Modulus (B), Shear Modulus (G), Young's Modulus (E), and Vickers Hardness (H_v) of *Cmcm*-CHC, *Cmmm*-CHC, Graphene, Diamond, and Other Carbon Materials[a]

	Cmcm-CHC	*Cmmm*-CHC	$P6_3/mmc$-CHC	*P6/mmm*-CHC	graphene	diamond	other carbon materials
B	313	190	324	195		432[c]	
G	289	164	302	126		519[c]	
E	663	383	691	312	1024[b]	1220[d]	
H_v	47	30	49	17		93[c]	84−96[e]

[a]The units of B, E, G, and H_v are GPa. [b]Density functional theory (DFT) calculations in ref 44. [c]DFT calculations in ref 5. [d]Ref 45. [e]Ref 43.

432 GPa and G 519 GPa).[5] The Young's modulus E is evaluated using the equation $E = -9BG/(3B + G)$.[39,40] *Cmcm*-CHC possesses the highest E among all these stable CHC structures (Table 2). The Vickers hardness H_v, which reflects elastic and plastic properties, is determined by the formula[41] $H_v = 2(k^2G)^{0.585} - 3$, where $k = G/B$ is Pugh's modulus ratio. The H_v for *Cmcm*-CHC, *Cmmm*-CHC, $P6_3/mmc$-CHC, and *P6/mmm*-CHC are 47, 30, 49, and 17 GPa, respectively. It should be emphasized that the ultrahigh H_v values for *Cmcm*-CHC and $P6_3/mmc$-CHC are 47 and 49 GPa, which are higher than the critical value (40 GPa[42]) for a superhard material. These values are much lower than those of diamond (93 GPa)[5] and also lower than those of carbon materials (84−96 GPa)[43] (Table 2). The results suggest that *Cmcm*-CHC and $P6_3/mmc$-CHC as superhard materials can be widely used in cutting and polishing wear-resistant coatings.

CONCLUSIONS

In this work, we unveil the phase transition and negative Poisson's ratio mechanism of CHCs by first-principles calculations. The NPR phenomenon in *Cmcm*-CHC and *Cmmm*-CHC occurs along the tube axis and armchair direction, respectively. It occurs mainly due to elongation of the angle and bond length to accommodate the external tension for *Cmcm*-CHC and the angle-dominant deformation for *Cmmm*-CHC. Meanwhile, a semimetal to semiconductor phase transition of *Cmcm*-CHC and *Cmmm*-CHC is observed by external strain along the armchair direction and tube axis, which stems from the new C1−C2 bond formation under tensile loading. Interestingly, the elastic properties show that *Cmcm*-CHC and $P6_3/mmc$-CHC are superhard materials. These outstanding properties render CHCs as an outstanding 3D nanomaterial with great promise for application in novel nanodevices.

ASSOCIATED CONTENT

Supporting Information

The Supporting Information is available free of charge at https://pubs.acs.org/doi/10.1021/acsomega.1c00718.

Details of the computation details, validation of the theoretical calculations, structure parameters of CHCs, Poisson's ratio, and phonon dispersions (PDF)

AUTHOR INFORMATION

Corresponding Authors

Shuaiwei Wang − *Henan Provincial Key Laboratory of Nanocomposites and Applications, Institute of Nanostructured Functional Materials, Huanghe Science and Technology College, Zhengzhou 450006, Henan, China*; orcid.org/0000-0003-2409-9888; Email: shuaiweiwang@hotmail.com

Baocheng Yang − *Henan Provincial Key Laboratory of Nanocomposites and Applications, Institute of Nanostructured Functional Materials, Huanghe Science and Technology College, Zhengzhou 450006, Henan, China*; Email: baochengyang@yahoo.cn

Author

Yanchun Li − *Henan Provincial Key Laboratory of Nanocomposites and Applications, Institute of Nanostructured Functional Materials, Huanghe Science and Technology College, Zhengzhou 450006, Henan, China*

Complete contact information is available at: https://pubs.acs.org/10.1021/acsomega.1c00718

Notes

The authors declare no competing financial interest.

ACKNOWLEDGMENTS

This work was financially supported by the National Natural Science Foundation of China (No. 51872110).

REFERENCES

(1) Novoselov, K. S.; Geim, A. K.; Morozov, S. V.; Jiang, D.; Zhang, Y.; Dubonos, S. V.; Grigorieva, I. V.; Firsov, A. A. Electric field effect in atomically thin carbon films. *Science* **2004**, *306*, 666−669.

(2) Wang, Z.; Zhou, X.; Zhang, X.; Zhu, Q.; Dong, H.; Zhao, M.; Oganov, A. R. Phagraphene: a low-energy graphene allotrope composed of 5−6−7 carbon rings with distorted dirac cones. *Nano Lett.* **2015**, *15*, 6182−6186.

(3) Wang, S.; Fan, Z.; Cui, Y.; Zhang, S.; Yang, B.; Chen, H. Fracture behaviors of brittle and ductile 2D carbon structures under uniaxial tensile stress. *Carbon* **2017**, *111*, 486−492.

(4) Jiang, J.; Leng, J.; Li, J.; Guo, Z.; Chang, T.; Guo, X.; Zhang, T. Twin graphene: A novel two-dimensional semiconducting carbon allotrope. *Carbon* **2017**, *118*, 370−375.

(5) Zhong, C.; Chen, Y.; Xie, Y.; Yang, S. A.; Cohen, M. L.; Zhang, S. Towards three-dimensional Weyl-surface semimetals in graphene networks. *Nanoscale* **2016**, *8*, 7232−7239.

(6) Krainyukova, N. V.; Zubarev, E. N. Carbon honeycomb high capacity storage for gaseous and liquid species. *Phys. Rev. Lett.* **2016**, *116*, No. 055501.

(7) Wang, S.; Yang, B.; Chen, H.; Ruckenstein, E. Popgraphene: a new 2D planar carbon allotrope composed of 5−8−5 carbon rings for high-performance lithium-ion battery anodes from bottom-up programming. *J. Mater. Chem. A* **2018**, *6*, 6815−6821.

(8) Geim, A. K. Graphene: status and prospects. *Science* **2009**, *324*, 1530−1534.

(9) Geim, A. K.; Novoselov, K. S. The rise of graphene. *Nat. Mater.* **2007**, *6*, 183−191.

(10) Bunch, J. S.; Van Der Zande, A. M.; Verbridge, S. S.; Frank, I. W.; Tanenbaum, D. M.; Parpia, J. M.; Craighead, H. G.; McEuen, P. L. Electromechanical resonators from graphene sheets. *Science* **2007**, *315*, 490−493.

(11) Li, D.; Kaner, R. B. Graphene-based materials. *Science* **2008**, *320*, 101.

(12) Wu, D.; Wang, S.; Yuan, J.; Yang, B.; Chen, H. Modulation of the electronic and mechanical properties of phagraphene via hydrogenation and fluorination. *Phys. Chem. Chem. Phys.* **2017**, *19*, 11771−11777.
(13) Baimova, J. A.; Rysaeva, L. K.; Liu, B.; Dmitriev, S. V.; Zhou, K. From flat graphene to bulk carbon nanostructures. *Phys. Status Solidi B* **2015**, *252*, 1502−1507.
(14) Pang, Z.; Gu, X.; Wei, Y.; Yang, R.; Dresselhaus, M. S. Bottom-up design of three-dimensional carbon-honeycomb with superb specific strength and high thermal conductivity. *Nano Lett.* **2017**, *17*, 179−185.
(15) Wang, S.; Wu, D.; Yang, B.; Ruckenstein, E.; Chen, H. Semimetallic carbon honeycombs: new three-dimensional graphene allotropes with Dirac cones. *Nanoscale* **2018**, *10*, 2748−2754.
(16) Lakes, R. Foam Structures with a Negative Poisson's Ratio. *Science* **1987**, *235*, 1038−1040.
(17) Wojciechowski, K. W. Constant thermodynamic tension Monte Carlo studies of elastic properties of a two-dimensional system of hard cyclic hexamers. *Mol. Phys.* **1987**, *61*, 1247−1258.
(18) Wojciechowski, K. W. Two-dimensional isotropic system with a negative poisson ratio. *Phys. Lett. A* **1989**, *137*, 60−64.
(19) Evans, K. E.; Nkansah, M. A.; Hutchinson, I. J.; Rogers, S. C. Molecular network design. *Nature* **1991**, *353*, 124.
(20) Tretiakov, K. V.; Wojciechowski, K. W. Monte Carlo simulation of two-dimensional hard body systems with extreme values of the Poisson's ratio. *Phys. Status Solidi B* **2005**, *242*, 730−741.
(21) Yao, Y. T.; Alderson, A.; Alderson, K. L. Can nanotubes display auxetic behaviour? *Phys. Status Solidi B* **2008**, *245*, 2373−2382.
(22) Jiang, J.; Chang, T.; Guo, X.; Park, H. S. Intrinsic negative Poisson's ratio for single-layer graphene. *Nano Lett.* **2016**, *16*, 5286−5290.
(23) Grima, J. N.; Winczewski, S.; Mizzi, L.; Grech, M. C.; Cauchi, R.; Gatt, R.; Attard, D.; Wojciechowski, K. W.; Rybicki, J. Tailoring Graphene to Achieve Negative Poisson's Ratio Properties. *Adv. Mater.* **2015**, *27*, 1455−1459.
(24) Jiang, J.; Park, H. S. Negative poisson's ratio in single-layer graphene ribbons. *Nano Lett.* **2016**, *16*, 2657−2662.
(25) Ho, D. T.; Nguyen, C. T.; Kwon, S.; Kim, S. Y. Auxeticity in Metals and Periodic Metallic Porous Structures Induced by Elastic Instabilities. *Phys. Status Solidi B* **2019**, *256*, No. 1800122.
(26) Ho, D. T.; Park, S.; Kwon, S.; Park, K.; Kim, S. Y. Negative Poisson's ratios in metal nanoplates. *Nat. Commun.* **2014**, *5*, No. 3255.
(27) Zhang, S.; Zhou, J.; Wang, Q.; Chen, X.; Kawazoe, Y.; Jena, P. Penta-graphene: A new carbon allotrope. *Proc. Natl. Acad. Sci. U.S.A.* **2015**, *112*, 2372−2377.
(28) Wang, S.; Peng, Z.; Fang, D.; Chen, S. A new Dirac nodal-ring semimetal made of 3D cross-linked graphene networks as lithium ion battery anode materials. *Nanoscale* **2020**, *12*, 12985−12992.
(29) Wang, W.; He, C.; Xie, L.; Peng, Q. The Temperature-Sensitive Anisotropic Negative Poisson's Ratio of Carbon Honeycomb. *Nanomaterials* **2019**, *9*, No. 487.
(30) Wang, S.; Si, Y.; Yang, B.; Ruckenstein, E.; Chen, H. Two-Dimensional Carbon-Based Auxetic Materials for Broad-Spectrum Metal-Ion Battery Anodes. *J. Phys. Chem. Lett.* **2019**, *10*, 3269−3275.
(31) Wang, B.; Wu, Q.; Zhang, Y.; Ma, L.; Wang, J. Auxetic B4N Monolayer: A Promising 2D Material with in-Plane Negative Poisson's Ratio and Large Anisotropic Mechanics. *ACS Appl. Mater. Interfaces* **2019**, *11*, 33231−33237.
(32) Peng, R.; Ma, Y.; He, Z.; Huang, B.; Kou, L.; Dai, Y. Single-Layer Ag2S: A Two-Dimensional Bidirectional Auxetic Semiconductor. *Nano Lett.* **2019**, *19*, 1227−1233.
(33) Wei, Q.; Yang, G.; Peng, X. Auxetic Tetrahex Carbon with Ultrahigh Strength and a Direct Band Gap. *Phys. Rev. Appl.* **2020**, *13*, No. 034065.
(34) Yuan, J.; Xue, K.; Wang, J.; Miao, X. Gallium Thiophosphate: An Emerging Bidirectional Auxetic Two-Dimensional Crystal with Wide Direct Band Gap. *J. Phys. Chem. Lett.* **2019**, *10*, 4455−4462.
(35) Wei, Y.; Wu, J.; Yin, H.; Shi, X.; Yang, R.; Dresselhaus, M. The nature of strength enhancement and weakening by pentagon−heptagon defects in graphene. *Nat. Mater.* **2012**, *11*, 759−763.
(36) Chen, Y.; Sun, Y.; Wang, H.; West, D.; Xie, Y.; Zhong, J.; Meunier, V.; Cohen, M. L.; Zhang, S. Carbon kagome lattice and orbital-frustration-induced metal-insulator transition for optoelectronics. *Phys. Rev. Lett.* **2014**, *113*, No. 085501.
(37) Adams, G. B.; O'Keeffe, M.; Demkov, A. A.; Sankey, O. F.; Huang, Y. Wide-band-gap Si in open fourfold-coordinated clathrate structures. *Phys. Rev. B* **1994**, *49*, 8048.
(38) Liu, H.; Neal, A. T.; Zhu, Z.; Luo, Z.; Xu, X.; Tománek, D.; Peide, D. Y. Phosphorene: an unexplored 2D semiconductor with a high hole mobility. *ACS Nano* **2014**, *8*, 4033−4041.
(39) Hill, R. The elastic behaviour of a crystalline aggregate. *Proc. Phys. Soc. A* **1952**, *65*, 349.
(40) Reuss, A. Berechnung der Fließgrenze von Mischkristallen auf Grund der Plastizitätsbedingung für Einkristalle. *Z. Angew. Math. Mech.* **1929**, *9*, 49−58.
(41) Chen, X.; Niu, H.; Li, D.; Li, Y. Modeling hardness of polycrystalline materials and bulk metallic glasses. *Intermetallics* **2011**, *19*, 1275−1281.
(42) Qin, J.; He, D.; Wang, J.; Fang, L.; Lei, L.; Li, Y.; Hu, J.; Kou, Z.; Bi, Y. Is rhenium diboride a superhard material? *Adv. Mater.* **2008**, *20*, 4780−4783.
(43) Yang, X.; Lv, C.; Liu, S.; Zang, J.; Qin, J.; Du, M.; Yang, D.; Li, X.; Liu, B.; Shan, C. Orthorhombic C14 carbon: A novel superhard sp3 carbon allotrope. *Carbon* **2020**, *156*, 309−312.
(44) Sun, H.; Mukherjee, S.; Singh, C. V. Mechanical properties of monolayer penta-graphene and phagraphene: a first-principles study. *Phys. Chem. Chem. Phys.* **2016**, *18*, 26736−26742.
(45) Spear, K. E.; Dismukes, J. P. *Synthetic Diamond: Emerging CVD Science and Technology*; John Wiley & Sons, 1994; Vol. *25*, p 315.

https://doi.org/10.1021/acsomega.1c00718
ACS Omega 2021, 6, 14896−14902